Self-Commissioning of Permanent Magnet Synchronous Machine Drives at Standstill Considering Inverter Nonlinearities

Gaolin Wang, *Member, IEEE*, Lizhi Qu, Hanlin Zhan, Jin Xu, Li Ding, Guoqiang Zhang, and Dianguo Xu, *Senior Member, IEEE*

***Abstract*—Offline parameter identification of permanent magnet synchronous machines (PMSMs) is essential for proper tuning of the controller and position observer for general-purpose drives with sensorless control. This paper proposes a self-commissioning method of electrical machine parameters at standstill only using a voltage source inverter fed drive. The influence of inverter nonlinearities including the effect of parasitic capacitance, which may cause estimation error, is analyzed. And an error model of inductance identification considering different rotor positions is established. Along with high-frequency sinusoidal signal, a supplementary direct current signal is injected into the estimated direct-axis to attenuate the inductance identification error. In addition, a compensation strategy based on the error model is adopted to enhance the accuracy of inductance identification. For stator resistance identification, the linear regression method is adopted to overcome the influence of inverter nonlinearities by injecting the linearly increasing current signal. The proposed method is promising and robust to extract the resistance information from the gradient coefficient of the voltage variation. The effectiveness of the proposed self-commissioning scheme is validated on a 22-kW PMSM drive.**

***Index Terms*—Inverter nonlinearities, linear regression, permanent magnet synchronous machine (PMSM), self-commissioning, standstill, voltage source inverter (VSI).**

I. Introduction

Permanent magnet synchronous machines (PMSMs) have been drawing increasing attention due to high efficiency, high-power factor and good dynamic performance, etc. [1]–[7]. In recent years, position sensorless PMSM control using the machine itself for sensing has been a research focus in industry applications [8]–[16]. Therefore self-commissioning of PMSMs at standstill using a voltage source inverter (VSI) fed drive without any extra hardware has been an emerging demand for the general-purpose drive applications. Since accurate offline identification of stator resistance, direct-quadrature $(d–q)$ axis inductances is necessary for proper tuning of the system controller and the position acquirement of electromotive force (EMF) model-based sensorless control [11]–[16], the critical parameters should be obtained before motor startup, otherwise the system would perform unwanted behavior or fail to operate. Especially, when self-commissioning at standstill is indispensable for some applications with load connected, it is not permissible to estimate parameters in rotating state or make the rotor deviate from the initial position. Self-commissioning of induction Motors (IMs) at standstill has been successfully applied in general-purpose drives [17], [18]. However, the identification methods for IMs are not compatible for PMSMs due to the existence of permanent magnet in the rotor. In order to integrate the PMSM sensorless control into general-purpose drives, offline parameter identification of PMSMs at standstill using VSI needs further research.

Offline parameter identifications of PMSMs can be generally classified into two different approaches. The first one focuses on the frequency domain, which mainly adopts the standard standstill frequency-response (SSFR) method [19]–[22]. In [19], SSFR method was performed on an axial flux interior PMSM (IPMSM) to evaluate the $d–q$ axis equivalent circuit parameters. To shorten the required time for SSFR test, a method using the multisinusoidal test signals was proposed in [20]. In this identification scheme, the test signals generated from the VSI were injected into the PMSM, and a measurement system was used to obtain the machine response and calculate the parameters. SSFR methods can achieve high identification accuracy but usually require extra instruments for measuring.

The second approach takes advantage of time-domain information for identification, for example, calculating machine parameters based on the time-domain response of an imposed perturbation, and measuring parameters according to the motor model [23]–[26]. In [24], a $d–q$ axis equivalent parameter estimation method of a synchronous generator adopting a novel standstill time-domain test with the sine cardinal perturbation was introduced. In [25], an offline identification scheme in rotating state was presented to identify the motor parameters accurately even though there were lots of harmonics in the motor. A standstill chirp test was introduced for parameter estimation of a synchronous generator using genetic and quasi-Newton algorithms, and a virtual instrument was developed to ensure the implementation of the chirp test [26]. Most

Manuscript received August 19, 2013; revised October 22, 2013 and December 23, 2013; accepted February 5, 2014. Date of publication February 17, 2014; date of current version August 13, 2014. This work was supported by the Research Fund for the National Science Foundation of China (51207030) and the Postdoctoral Science-Research Developmental Foundation of Heilongjiang Province (LBH-Q12087). Recommended for publication by Associate Editor A. M. Trzynadlowski.

The authors are with the School of Electrical Engineering and Automation, Harbin Institute of Technology, Harbin 150001, China (e-mail: WGL818@hit.edu.cn; 345225537@qq.com; shintar521@gamil.com; 670544208@qq.com; dl7484650@163.com; wisdom9527@163.com; xudiang@hit.edu.cn).

Color versions of one or more of the figures in this paper are available online at http://ieeexplore.ieee.org.

Digital Object Identifier 10.1109/TPEL.2014.2306734

of the time-domain-based methods focus on parameter testing with supplementary instruments to obtain the characteristics of the machine model. Moreover, the inverter nonlinearities cause voltage error between the reference and the output [27], [28], which deteriorates the accuracy of parameter identification [29]. A least square algorithm based startup parameter identification method was introduced in [30] which considered the inverter nonlinearities and took advantage of the current injection transient process. For general-purpose drive applications, the testing condition is not always available, and all the parameter identification algorithms should be realized just by the digital signal processor (DSP) in the drives.

A novel self-commissioning methodology for PMSMs at standstill is proposed in this paper, which requires no additional hardware but only a VSI. The main contribution is the proposed inductance parameter identification method considering detailed identification error analysis of inverter nonlinearity influence at different rotor positions. After estimating the initial rotor position, the inductances are identified by injecting high-frequency signal in the estimated d- and q-axes, respectively. The proposed inductance identification belongs to the frequency-domain approach. Additionally, a supplementary dc current is injected into the d-axis to attenuate the influence of the inverter nonlinearities and keep the rotor at the initial position. Furthermore, the identified inductance results are compensated through a nonlinear model considering the parasitic capacitance effect and the influence of cross coupling is analyzed and tested. In order to diminish the influence of the inverter nonlinearities during the resistance identification, a linear regression-based resistance identification methodology is proposed by injecting a linearly increasing current in d-axis. Due to the induction machine, winding resistance identification methods [31]–[33] by injecting current in any two phases or three phases cause the alignment torque that induces the rotor of PMSM to rotate, the space current vector injected in d-axis is proposed to address this issue. Moreover, the linear regression method owns good robustness and can utilize multipoint information. Finally, the proposed self-commissioning methodology is validated on a 22-kW-interior PMSM (IPMSM) platform.

II. Proposed Inductance Identification Methodology

A. Proposed Scheme of d-q Axis Inductance Identification

The VSI is used for the self-commissioning at standstill. For a position sensorless PMSM drive, the initial rotor position should be estimated before parameter identification. In this scheme, the initial position estimation method proposed in [34] is adopted. HF carrier signal injection is employed to identify the magnetic pole position, and two short voltage pulses are injected to determine the rotor polarity. Ultimately, the rotor position θ_r can be acquired at standstill before the parameter identification.

The proposed offline inductance identification scheme is shown in Fig. 1. The d- or q-axes inductance identification is selected through the terminal 1 or 2 correspondingly. For the d-axis inductance L_d identification, a supplementary dc current is injected into the estimated d-axis using the current closed-loop control. And a HF sinusoidal voltage signal is superposed

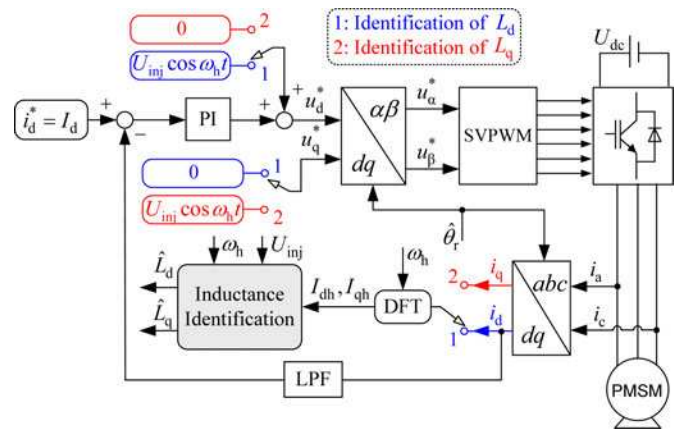

Fig. 1. Proposed scheme of $d-q$ axis inductance identification.

upon the output of d-axis current regulator. The dc current can attenuate the influence of inverter nonlinearities.

The d-axis voltage equation in the synchronous rotating reference frame can be represented as

$$u_d = R_s i_d + p\varphi_d - \omega_e \varphi_q \tag{1}$$

where R_s is the stator resistance, u_d and i_d are the d-axis voltage and current, φ_d and φ_q are the $d-q$ axis flux linkages, p is the differential operator, ω_e is the electrical angular velocity, and it is equal to zero because the rotor is kept at standstill. Then, (1) can be expressed as

$$u_d = \frac{d\varphi_d}{dt} + R_s i_d = \frac{d\left(L_d i_d + \varphi_f\right)}{dt} + R_s i_d = \frac{d\left(L_d i_d\right)}{dt} + R_s i_d. \tag{2}$$

The d-axis current response should be extracted according to (2), and its amplitude can be calculated by adopting discrete Fourier transform. The amplitude of excited HF current can be obtained from

$$\begin{cases} R_1 = \dfrac{2}{N}\left[x(0) + \displaystyle\sum_{i=1}^{N-1} x[i]\cos\frac{2\pi i}{N}\right] \\ I_1 = \dfrac{2}{N}\left[-\displaystyle\sum_{i=1}^{N-1} x[i]\sin\frac{2\pi i}{N}\right] \\ I_{dh} = \sqrt{R_1^2 + I_1^2} \end{cases} \tag{3}$$

where R_1 and I_1 are the real and imaginary components of the HF current, respectively.

Therefore, d-axis inductance can be estimated as

$$\hat{L}_d = \frac{U_{\mathrm{inj}}}{I_{dh}\omega_h} \tag{4}$$

where the symbol "^" means the estimated value, U_{inj} and ω_h are the amplitude and frequency of the injected HF signal, respectively. This estimated value is not the final identified inductance because of the stator resistance and the current distortion during the injection process. It will be compensated through an inverter nonlinearity model including the influence of stator resistance in Part B.

During L_q identification, it might cause a biggish pulsating torque by injecting a HF current in q-axis. But the self-lock

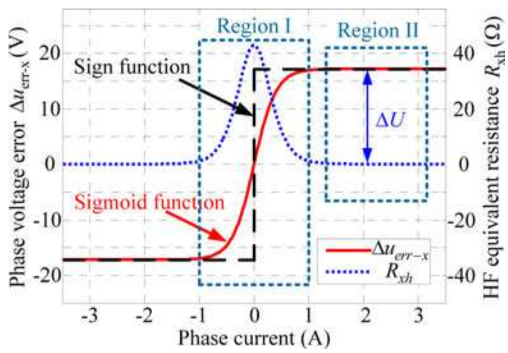

Fig. 2. Phase voltage error and the HF equivalent resistance.

can be guaranteed by injecting a dc current in d-axis to keep the rotor at standstill, and then a HF sinusoidal voltage signal is superposed upon the output of q-axis current regulator to acquire the inductance parameter. The signal process of L_q identification is similar to that of L_d shown in (3) and (4).

B. Error Analysis of the d-Axis Inductance Identification

Voltage error characteristic of the inverter nonlinearities at fundamental-frequency operation can be generally formulated through the saturation function concerning the phase current [35]. For HF signal injection, this description can not completely indicate the nonlinearity characteristic [36]. A more accurate model was proposed in [37] and [38], where the HF equivalent resistance was introduced. And this model employed small signal linearization to simplify the analysis of nonlinearities. The influence is depicted more precisely when the phase current is near to zero. The voltage error $\Delta u_{\text{err}-x}$ in arbitrary phase can be expressed as

$$\Delta u_{\text{err}-x} \approx f(i_{xf}) + f'(i_{xf}) \cdot i_{xh} \approx \text{sign}(i_{xf}) \cdot \Delta U + R_{xh} \cdot i_{xh} \tag{5}$$

where i_{xf} denotes the fundamental current of arbitrary phase x, ΔU denotes the saturation value of the voltage error in region II of Fig. 2, and R_{xh} denotes the HF equivalent resistance that is a nonlinear variable related to i_{xf}.

As in [38], the voltage error of the fundamental component can be expressed as

$$\Delta u_{\text{err}-x} = f(i_{xf}) = 2\Delta U \left(\frac{1}{1+e^{-ki_{xf}}} - \frac{1}{2} \right). \tag{6}$$

It offers more information of the parasitic capacitance affecting inductance identification in region I of Fig. 2. R_{xh} depends on the characteristic of insulated gate bipolar transistor (IGBT), and it can be approximated as

$$R_{xh} = f'(i_{xf}) = \frac{2\Delta U \cdot k \cdot e^{-ki_{xf}}}{(1+e^{-ki_{xf}})^2} \tag{7}$$

where k is a model parameter only determined by the dead time and the device characteristic. Under the condition of $U_{\text{dc}} = 537$ V and the dead time 3.2 μs, $k = 0.6$ and $\Delta U = 17.2$ V can be obtained. Then, $\Delta u_{\text{err}-x}$ and R_{xh} are described in Fig. 2. The way to obtain the coefficients k and ΔU is the same as the thought in [35].

The HF voltage signal superposed on the d-axis winding can be expressed as

$$u_d^* = U_{\text{inj}} \cos(\omega_h t). \tag{8}$$

And the current response of d-axis will be

$$i_h = I_h \sin(\omega_h t + \varphi) \tag{9}$$

where φ is the phase shift caused by the inverter nonlinearities and the winding resistance that will be addressed later.

The voltage error generated from R_{xh} can be calculated by i_h, and the d-axis voltage error can be derived through rotating coordinate transformation. The analysis of L_d estimation error due to inverter nonlinearities is as follows.

The dc current offset superposed in the d-axis can improve the identification accuracy by pulling the stator current out of the zero current clamping (ZCC) zone. The whole current response at the $d-q$ axes can be given as

$$\begin{cases} i_d = i_h + I_d = I_h \sin(\omega_h t + \varphi) + I_d \\ i_q = 0. \end{cases} \tag{10}$$

Since the dc component keeps constant at the same rotor position, the corresponding voltage error is also constant, whereby the fundamental voltage error has no impact on the result. Only the influence of the voltage error induced from i_h needs to be considered. The $d-q$ axis HF voltage errors can be represented as

$$\begin{cases} \Delta U_{\text{err}-dh} = \dfrac{2}{3} i_h \left[R_{ah} \cos^2(\theta_r) + R_{bh} \cos^2\left(\theta_r - \dfrac{2}{3}\pi\right) \right. \\ \qquad \left. + R_{ch} \cos^2\left(\theta_r + \dfrac{2}{3}\pi\right) \right] \\ \Delta U_{\text{err}-qh} = \dfrac{1}{3} i_h \left[R_{ah} \sin(2\theta_r) + R_{bh} \sin 2\left(\theta_r - \dfrac{2}{3}\pi\right) \right. \\ \qquad \left. + R_{ch} \sin 2\left(\theta_r + \dfrac{2}{3}\pi\right) \right]. \end{cases} \tag{11}$$

Therefore, the HF equivalent resistances in $d-q$ axes are

$$\begin{cases} R_{dh} = \dfrac{2}{3} \left[R_{ah} \cos^2(\theta_r) + R_{bh} \cos^2\left(\theta_r - \dfrac{2}{3}\pi\right) \right. \\ \qquad \left. + R_{ch} \cos^2\left(\theta_r + \dfrac{2}{3}\pi\right) \right] \\ R_{qh} = \dfrac{1}{3} \left[R_{ah} \sin(2\theta_r) + R_{bh} \sin 2\left(\theta_r - \dfrac{2}{3}\pi\right) \right. \\ \qquad \left. + R_{ch} \sin 2\left(\theta_r + \dfrac{2}{3}\pi\right) \right] \end{cases} \tag{12}$$

and the derivation of the HF equivalent resistances is shown in Appendix.

Only the d-axis voltage error needs to be concerned for L_d identification, the voltage error in q-axis would not affect the identification if the cross-coupling effect is neglected. By substituting (7) into (12), R_{dh} is portrayed in polar coordinate with an electrical cycle as shown in Fig. 3. According to Fig. 3(a), R_{dh} keeps constant if there is no additional dc current injected into the d-axis. From Fig. 3(b), R_{dh} decreases gradually with the increase of the injected d-axis dc current.

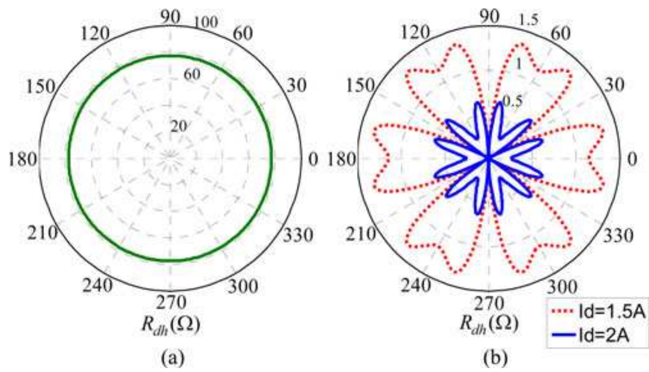

Fig. 3. HF equivalent resistance R_{dh} in polar coordinate with an electrical cycle. (a) $I_d = 0$, (b) $I_d = 1.5$ A and 2 A.

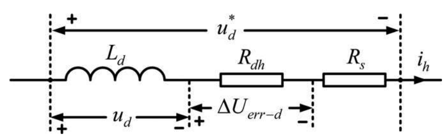

Fig. 4. HF equivalent circuit of L_d identification.

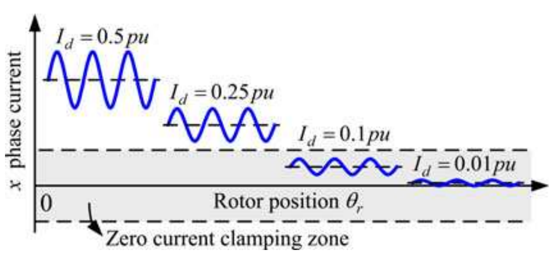

Fig. 5. HF current response of arbitrary phase during d-axis inductance identification.

Considering the nonlinearities of inverter, the actual output voltage on the d-axis winding amounts to

$$u_d = u_d^* - \Delta U_{\mathrm{err}-d}. \tag{13}$$

Therefore, the HF equivalent circuit of L_d identification can be described as Fig. 4.

Only u_d^* and i_h can be known when the identification algorithm is plunged into the commercial general-purpose drives. Considering the influence of R_{dh} as shown in Fig. 4, the obtained L_d can be given as

$$\hat{L}_d = \frac{\sqrt{(\omega_h^2 L_d^2 + R_{dh}^2 + R_s^2 + 2R_{dh}R_s)}}{\omega_h}. \tag{14}$$

Then, the estimation error of L_d can be obtained

$$\Delta L_d = L_d - \hat{L}_d = L_d - \frac{\sqrt{(\omega_h^2 L_d^2 + R_{dh}^2 + R_s^2 + 2R_{dh}R_s)}}{\omega_h}. \tag{15}$$

The phase-shifted angle φ in (10) is caused by the existence of R_s and R_{dh} due to the inverter nonlinearities. Assuming that the inverter nonlinearities do not exist, there will be no equivalent HF resistance in equivalent circuit. As shown in Fig. 5, if the dc component of an arbitrary phase current turns to zero, the HF component i_{xh} also becomes zero, which means the voltage drop on R_{xh} is zero. And the HF equivalent resistances of the other two phases are also nearly zero when their dc components are high enough to make them far away from the ZCC zone. Therefore, the HF current would not be distorted. In this case, no estimation error is induced for L_d identification.

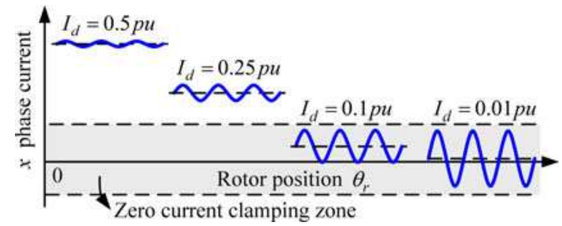

Fig. 6. HF current response of arbitrary phase during q-axis inductance identification.

C. Error Analysis of the q-Axis Inductance Identification

The same as the way to estimate the d-axis inductance, the identified q-axis inductance can be represented as

$$\hat{L}_q = \frac{U_{\mathrm{inj}}}{I_{qh}\omega_h}. \tag{16}$$

The injected d-axis dc component can partly let the HF current stay far away from ZCC zone. The amplitude of the HF current will be modulated by the rotor position as shown in Fig. 6, which is in an opposite way compared to Fig. 5.

The amplitude of HF current i_{xh} reaches the maximum if the dc component of that phase turns to zero. And i_{xh} diminishes with the dc component increase. Although i_{xh} will not be disturbed by the nonlinearities if the corresponding dc component reaches the maximum as shown in Fig. 3, its proportion of the q-axis HF current reduces nearly to zero and makes no contribution to L_q estimation. Whereas the ratios of HF currents in the other two phases, which are parts of the d-axis HF current response staying in ZCC zone are higher. In this case, the HF currents are distorted, which deteriorate the identification results.

As the estimation error analysis of L_d, the HF equivalent resistances can be expressed as

$$\begin{cases} R_{dh} = -\dfrac{1}{3}\Big[R_{ah}\sin(2\theta_r) + R_{bh}\sin 2\left(\theta_r - \dfrac{2}{3}\pi\right) \\ \qquad + R_{ch}\sin 2\left(\theta_r + \dfrac{2}{3}\pi\right)\Big] \\ R_{qh} = \dfrac{2}{3}\Big[R_{ah}\sin^2(\theta_r) + R_{bh}\sin^2\left(\theta_r - \dfrac{2}{3}\pi\right) \\ \qquad + R_{ch}\sin^2\left(\theta_r + \dfrac{2}{3}\pi\right)\Big]. \end{cases} \tag{17}$$

Neglecting the cross-coupling effect, the voltage error of d-axis would not affect the L_q identification. And R_{qh} portrayed in polar coordinate can be described as Fig. 7, where $k = 0.6$, $\Delta U = 17.2$ V, and $I_d = 0$, 0.5, and 2 A, respectively. From Fig. 7 when I_d is zero, R_{qh} in different positions stay constant that will cause lager estimation error. And there is a sixth pulsation in an electrical circle when I_d is not zero.

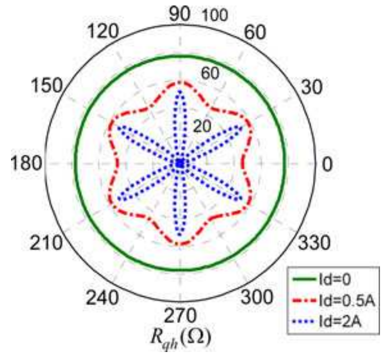

Fig. 7. HF equivalent resistance R_{qh} in polar coordinate with an electrical cycle.

Theoretically, if I_d is large enough, the zero error points will appear at $\theta_r = k\pi/3$, where $k \in \{0, 1, 2, 3, 4, 5\}$.

Considering the inverter nonlinearities, the actual voltage superposed on q-axis winding is

$$u_q = u_q^* - \Delta U_{\mathrm{err}-q}. \tag{18}$$

So the HF equivalent circuit of L_q identification can be described similarly as Fig. 4. Meanwhile, the identification error can be expressed as

$$\Delta L_q = L_q - \hat{L}_q = L_q - \frac{\sqrt{(\omega_h^2 L_q^2 + R_{qh}^2 + R_s^2 + 2R_{qh}R_s)}}{\omega_h}. \tag{19}$$

D. Compensation of the Estimated Inductances

In the process of the inductance identification, the injected dc current is fixed and the rotor position is obtained. In order to improve the identification accuracy, the error compensation can be achieved through (7), (12), (14), (15), (17), and (19). First, the equivalent phase HF resistance is calculated according to (7). Then, (12) is used to calculate the equivalent d-axis HF resistance for L_d identification, and (17) is for L_q identification. Finally, (15) and (19) are the compensation equations for d- and q-axis inductance identification, respectively.

E. Analysis of the Cross-Coupling Effects

According to the proposed identification method, for d-axis inductance identification, the high-frequency voltage equation can be expressed as

$$\begin{cases} u_{dh} = L_d \dfrac{di_{dh}}{dt} + L_{dq}\dfrac{di_{qh}}{dt} + i_{dh}R_s \\ 0 = L_q \dfrac{di_{qh}}{dt} + L_{qd}\dfrac{di_{dh}}{dt} + i_{qh}R_s \end{cases} \tag{20}$$

where L_{dq} and L_{qd} are the cross-coupling inductances.

Based on (20), the identified d-axis inductance can be represented as

$$\hat{L}_d \approx L_d - \frac{L_{dq}^2}{L_q} \tag{21}$$

where only the influence of cross-coupling inductance is concerned and assume $L_{dq} = L_{qd}$. In the same way, the identified q-axis inductance can be represented as

$$\hat{L}_q \approx L_q - \frac{L_{dq}^2}{L_d}. \tag{22}$$

It indicates that the cross-coupling effects influence the identified results. The extent of cross-coupling effects depends on the electrical machine design and operating current condition.

F. Design of PI Coefficients for d-Axis Current Regulator

As shown in Fig. 1, there is a current closed loop for injecting the dc current component in d-axis. Usually, in order to design the PI coefficients optimally, the machine parameters are demanded. However, the estimated machine parameters can be obtained after the parameter identification execution. In the proposed scheme, the rough parameters are derived according to the basic information from the rated values on the machine nameplate, including the rated power P_N, the rated current I_N, and the rated voltage U_N. Then, the practicable PI coefficients for d-axis current regulator can be obtained through the design.

The rated current I_N and the rated power P_N are known when an electric machine is given. Then, the resistance can be roughly calculated according to the loss equation

$$P_N \frac{1-\eta}{\eta}\gamma = 3I_N^2 R_s \tag{23}$$

where η denotes the efficiency and γ denotes the copper loss percentage of the total loss at rated operation point. When the efficiency of machine is not known exactly, it can be roughly estimated according to the rated power of the test machine. The general scope of γ is $1/2 \sim 2/3$, which has been investigated in many papers and motor design books, such as [39]. For the 22-kW PMSM adopted for experiment, the efficiency is chosen as 95% and the rated current is 37.2 A. The percentage coefficient γ is regarded as 0.5, and the resistance can be roughly estimated as 0.139 Ω, which is closed to the real value.

The rough inductance can be estimated according to the voltage equations in the d-q axes. Assume $L_m = L_d = L_q$ so that to estimate a rough value which is only used for regulator parameter design in the parameter identification process. The quadratic sum of the d-q axis voltage equations is

$$U_d^2 + U_q^2 = (R_s I_d + X_q I_q)^2 + (E_0 - I_d X_d + I_q R_s)^2 \tag{24}$$

where X_d and X_q are $d-q$ axis inductive reactances. Due to $I_d = 0$, $U_d^2 + U_q^2 = U_N^2$ and R_s has been obtained before, the back EMF can be estimated as

$$E_0 = \frac{P_N}{3I_N} \tag{25}$$

where P_N is 22 kW and the estimated back EMF is 197.13 V. Since $L_m = L_d = L_q$, i.e., $X_d = X_q = X_m$, the final equation for rough inductance calculation is

$$U_N^2 = (X_m I_q)^2 + (E_0 + I_q R_s)^2 \tag{26}$$

where I_q is 37.2 A and $U_N = 220$ V for the tested 22-kW IPMSM. So the derived inductance is 7.40 mH.

According to the obtained rough resistance and inductance, the PI coefficients of the d-axis current regulator can be designed

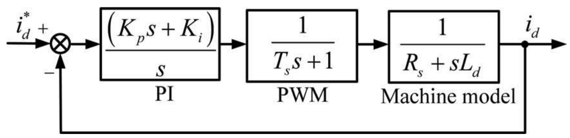

Fig. 8. Equivalent diagram of the d-axis current loop.

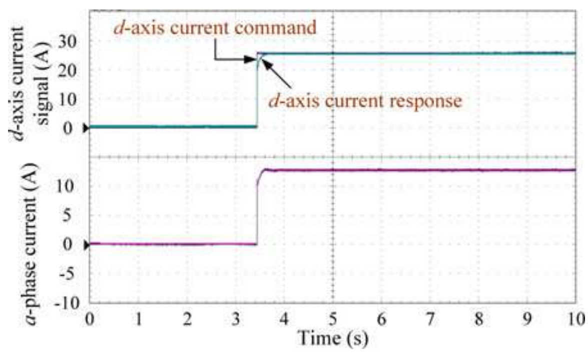

Fig. 9. Experimental results of step response of d-axis current loop for parameter identification.

for the offline parameter identification. The equivalent diagram of d-axis current loop is shown in Fig. 8. The PWM period and the closed-loop transfer function of d-axis current loop can be expressed as

$$\boldsymbol{G}(s) = \frac{i_d}{i_d^*} = \frac{K_p}{T_s L_d s^2 + L_d s + K_p}$$

where $K_i = \frac{R_s}{L_d} \cdot K_p$ and the term $T_s L_d s^2$ is so small in this situation that the closed-loop transfer function can be regarded as a first-order system

$$\boldsymbol{G}(s) = \frac{i_d}{i_d^*} = \frac{K_p}{L_d s + K_p} = \frac{K_p/L_d}{s + K_p/L_d}. \tag{27}$$

The term K_p/L_d in (27) indicates the bandwidth of the current loop. When there is a desired bandwidth of ω_{cb}^*, then the K_p can be obtained

$$\omega_{cb}^* = K_p/L_d \Rightarrow K_p = \omega_{cb}^* L_d. \tag{28}$$

So

$$K_i = \frac{R_s}{L_d} \cdot K_p = \frac{R_s}{L_d} \cdot \omega_{cb}^* L_d = R_s \omega_{cb}^*. \tag{29}$$

In the identification strategy, ω_{cb}^* is selected as $100^*2\pi$ rad/s because high control performance for the transient process is not required. Therefore, the PI coefficients can be obtained as $K_p = 4.9$ and $K_i = 83.33$. To verify the effectiveness of the design of the d-axis current regulator according to the estimated rough machine parameters, the current response of a step input is shown in Fig. 9.

In Fig. 9, from top to bottom, the d-axis current command, d-axis current response, and the a-phase current response are given, respectively. The d-axis current response is acceptable that it can be applied in this application. The derived resistance and inductance are rough and the initial PI coefficients are merely for the parameter identification. Once the more accurate parameters are identified, the refined PI coefficients could be calculated for the high-performance vector control system.

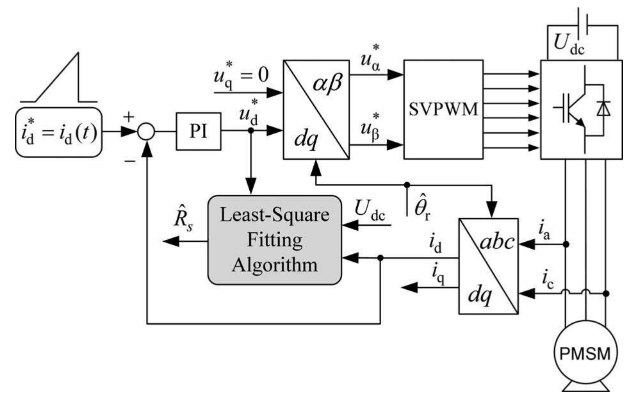

Fig. 10. Diagram of the stator resistance identification.

III. Proposed Stator Resistance Identification Methodology

A. Proposed Scheme of Stator Resistance Identification

Injecting two different dc currents is the conventional way to counteract the influence of the inverter nonlinearities. Then, the estimated resistance value can be calculated from dividing the reference voltage difference by the output current difference. All the above is based on the assumption that the equivalent voltage error of inverter nonlinearities is constant. The block diagram of the proposed R_s identification is shown in Fig. 10. The main contribution is taking advantage of linear regression to enhance the robustness against the inverter nonlinearities and undesired perturbations during the identification. A dc current with the gradually increasing amplitude is injected into the d-axis to identify R_s at standstill. And the current command in discrete form is selected as

$$i_{sd}^*(k+1) = i_{sd}^*(k) + \Delta i \tag{30}$$

where Δi denotes the incremental value of the current reference, $\Delta i = I_{\max}/n$, n is the number of the sampling points, and $I_{\max}$ is the maximum injected current.

The voltage error caused by the inverter nonlinearities will change obviously in the small current range due to the effect of the parasitic capacitance [27]. On account of the VSI nonlinearities, the starting sampling current point should be high enough to avoid this influence. The regression line is $u = f(i) = R_s i + \Delta u$ and after the regression, the corresponding coefficients can be obtained as

$$\begin{cases} \Delta u = \dfrac{\left(\sum_{j=1}^n u_j\right)\left(\sum_{j=1}^n i_j^2\right) - \left(\sum_{j=1}^n i_j\right)\left(\sum_{j=1}^n i_j u_j\right)}{n\left(\sum_{j=1}^n i_j^2\right) - \left(\sum_{j=1}^n i_j\right)^2} \\ \hat{R}_s = \dfrac{n\left(\sum_{j=1}^n i_j u_j\right) - \left(\sum_{j=1}^n i_j\right)\left(\sum_{j=1}^n u_j\right)}{n\left(\sum_{j=1}^n i_j^2\right) - \left(\sum_{j=1}^n i_j\right)^2} \end{cases} \tag{31}$$

where Δu is the equivalent voltage error of the VSI, i_j and u_j are the injected current and the reconstructed output voltage at the sampling point, respectively.

The robustness of the R_s identification can be improved by using the linear regression for the gradient calculation according to the multipoint information. In this way, the gradient of the identification line is the stator resistance and the error induced from inverter nonlinearities could be resisted effectively.

B. Error Analysis of the Stator Resistance Identification

There is only DC signal injected, so the phase voltage error caused by the parasitic capacitance can be as (6). The relation between the voltage error vector angle γ and the amplitude $\Delta U_{\mathrm{err-syn}}$ in vector form can be obtained by modeling the synthetic vector, where γ is defined as the phase lead of the voltage error vector to the *a*-axis. The voltage error vector is defined as

$$\begin{aligned}\boldsymbol{u}_{\mathrm{err-syn}} &= \frac{2}{3}(\Delta U_{\mathrm{err-}a} + \Delta U_{\mathrm{err-}b}\cdot e^{j120^\circ} + \Delta U_{\mathrm{err-}c}\cdot e^{j240^\circ})\\ &= \Delta U_{\mathrm{err-syn}}\cdot e^{j\gamma}\end{aligned} \tag{32}$$

where $\Delta U_{\mathrm{err-syn}}$ and γ satisfy (33) and (34), respectively,

$$\begin{cases}\Delta U_{\mathrm{err-syn}} = \dfrac{2}{3}\left[\left(\Delta U_{\mathrm{err-}a} - \dfrac{1}{2}\Delta U_{\mathrm{err-}b} - \dfrac{1}{2}\Delta U_{\mathrm{err-}c}\right)^2 \right.\\ \qquad\qquad \left. + \left(\dfrac{\sqrt{3}}{2}\Delta U_{\mathrm{err-}b} - \dfrac{\sqrt{3}}{2}\Delta U_{\mathrm{err-}c}\right)^2\right]^{0.5}\\ \gamma_1 = \tan^{-1}\dfrac{\sqrt{3}\Delta U_{\mathrm{err-}b} - \sqrt{3}\Delta U_{\mathrm{err-}c}}{2\Delta U_{\mathrm{err-}a} - \Delta U_{\mathrm{err-}b} - \Delta U_{\mathrm{err-}c}}\end{cases} \tag{33}$$

$$\gamma = \begin{cases}\gamma_1, & \text{if } (\sqrt{3}\Delta U_{\mathrm{err-}b} - \sqrt{3}\Delta U_{\mathrm{err-}c}) > 0\\ \gamma_1 + \pi, & \text{if } (\sqrt{3}\Delta U_{\mathrm{err-}b} - \sqrt{3}\Delta U_{\mathrm{err-}c}) < 0.\end{cases} \tag{34}$$

Based on (33) and (34), the voltage error vector angle γ and amplitude $\Delta U_{\mathrm{err-syn}}$ are shown in Fig. 11(a) and (b), respectively. According to the simplified error model, the phase voltage error $U_{\mathrm{err-}x}$ can be described by a sign function. Then, the voltage error vector is one of the six constant space vectors. Using the accurate voltage error vector, $U_{\mathrm{err-}x}$ can be described by a sigmoid function. And the accurate voltage error vector is no more one of the six constant space vectors. As shown in Fig. 11, the dashed lines describe the angle and amplitude of the voltage error vector at different rotor positions.

The corresponding components of the voltage error vector decomposed into the *d*-*q* synchronous rotating coordinate are shown in Fig. 12. They describe the $d-q$ axis voltage errors at different current values and rotor positions. The amplitude of d-axis error trends to be constant if the injected d-axis dc current is high enough. The same tendency occurs in the q-axis error component. The characteristic shown in Fig. 12 properly explains why the resistance calculation should start from an enough high current point at a certain rotor position.

IV. Experimental Results

The proposed self-commissioning algorithm was validated on a 22-kW IPMSM drive based on DSP as shown in Fig. 13.

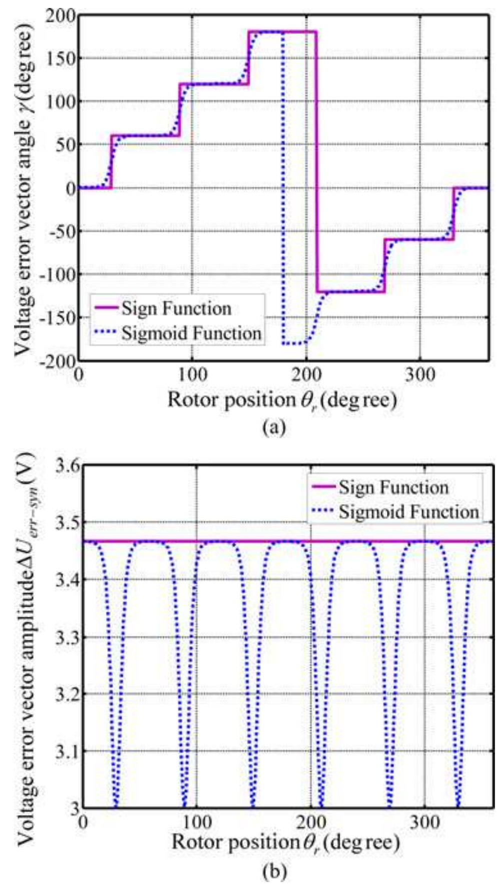

Fig. 11. Variation of voltage error vector versus rotor position. (a) The voltage error vector angle γ and (b) the voltage error vector amplitude $\Delta U_{\mathrm{err-syn}}$.

The rated parameters of the IPMSM are listed as follows: 380 V, 37.2 A, 50 Hz, 210 N·m, 1000 r/min. The nominal stator resistance measured by Micro-Ohm Resistance Meter (RM3544) is 0.135 Ω. The intelligent power module PM100RSE120 whose typical switching time $t_{\mathrm{on}} = 1.0$ μs and $t_{\mathrm{off}} = 2.5$ μs is used. The typical rated voltage drop of IGBT is 2.4 V and the typical rated voltage drop of diode is 2.5 V. The DSP TMS320F2808 is adopted to execute the whole parameter identification algorithm. The PWM switching frequency of the inverter is 10 kHz, and the dead time is set to 3.2 μs. The frequency of the injected HF voltage signal is 500 Hz. The current reference increases linearly at 0.0665 p.u./s during the resistance identification and the number of sampling points is 26. An absolute encoder (ECN1113) with 13-bit resolution is used to obtain the actual initial position that is solely used for comparison and not for parameter identification.

The a-phase current of the whole identification process is shown in Fig. 14. It includes the initial position estimation, $d-q$ axis inductance identification, and stator resistance identification. The initial rotor position estimation adopts the scheme in [34] by injecting HF carrier signal and two short voltage pulses. After obtaining the initial rotor position, the parameter identification can be performed and the rotor can be kept at standstill.

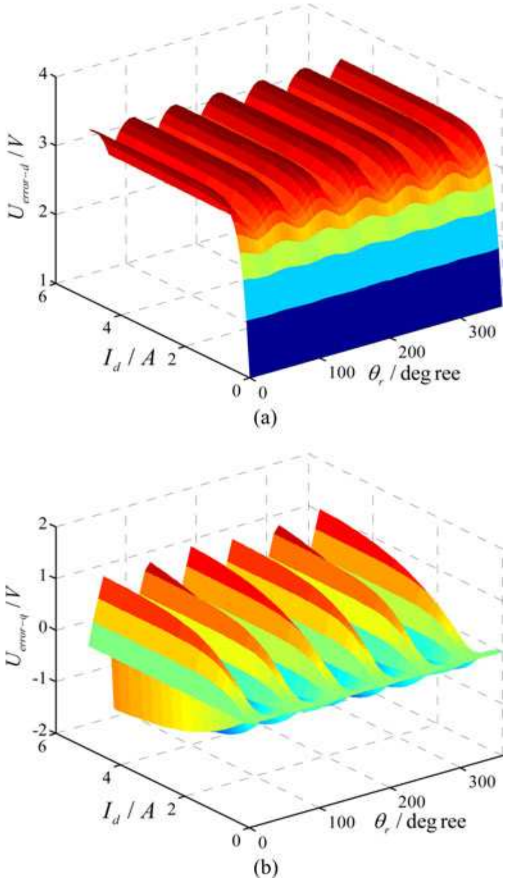

Fig. 12. Variation of voltage error vector decomposed into $d-q$ axes versus rotor position and injected dc current. (a) Amplitude of voltage error vector decomposed in d-axis, (b) amplitude of voltage error vector decomposed in q-axis.

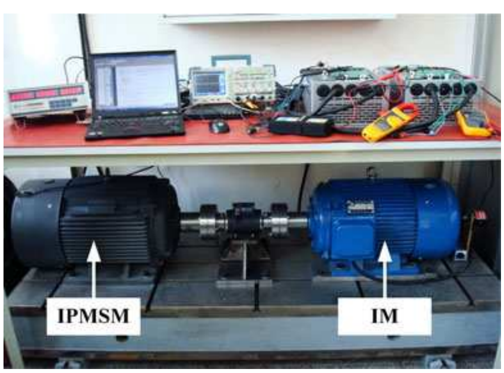

Fig. 13. Test platform of 22-kW PMSM.

In order to ensure the accuracy of the identification, the initial rotor position estimation should be precise enough. Fig. 15 shows the accuracy of the estimated initial rotor position. The electrical angle error is less than 5°, which means the estimated initial rotor position is qualified enough to the following parameter identification methodology.

Fig. 16 shows the $d-q$ axis inductance identification results at the initial position of 108°. From top to bottom, the estimated L_d, the a-phase current and the estimated L_q are given. The supplementary d-axis dc current is 0.25 p.u. The HF injected voltage

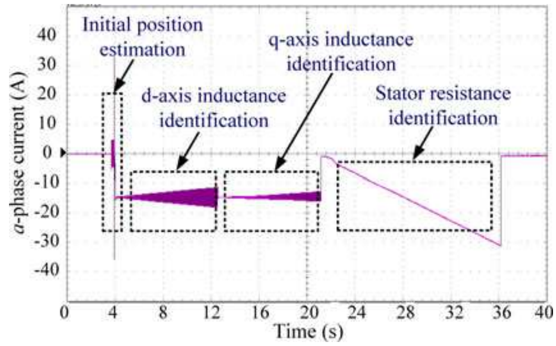

Fig. 14. a-phase current waveform of the whole offline identification.

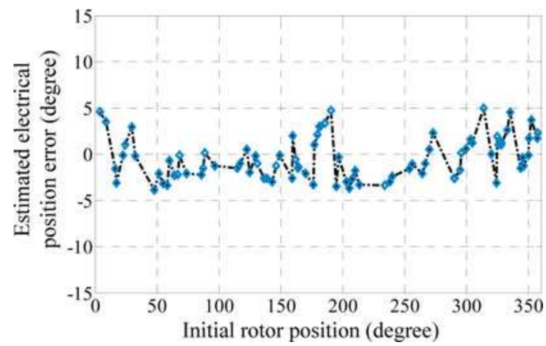

Fig. 15. Estimation error of the initial rotor position in electrical degree.

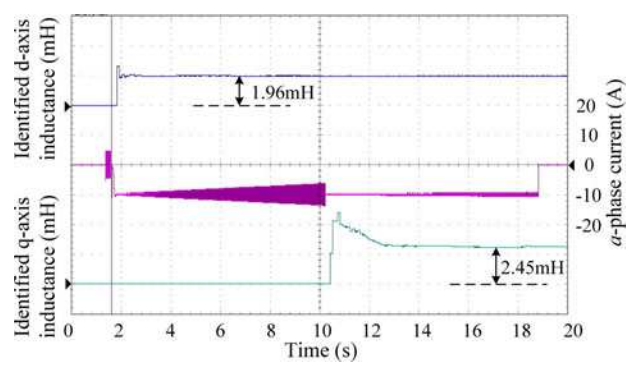

Fig. 16. Waveforms of the inductance identification results.

increases gradually to avoid producing overcurrent and ensure the intensity of signals. The d- and q-axes inductances converge to stable values with the increase of the injected current.

Fig. 17 shows the identified $d-q$ axis inductances at different initial angles (0°–360°) with different injected d-axis dc currents. The injected d-axis dc component is set to 0, 0.3, and 0.6 p.u., respectively, and the injected HF voltage is 0.1 p.u. From the results of Fig. 17(a), the HF equivalent resistance becomes constant when I_d equals zero, which means the error in polar coordinate is constant during a circle. When I_d is not zero, there are 12 pulsations in an electrical circle, which is consistent with Fig. 3(b). The estimation error approaches zero at $\theta_r = (2k+1)\pi/6, k \in \{0, 1, 2, 3, 4, 5\}$. Fig. 17(b) describes the identification results of q-axis inductance with different injected d-axis dc currents. When the injected dc current keeps constant, the maximum estimation error will be introduced at

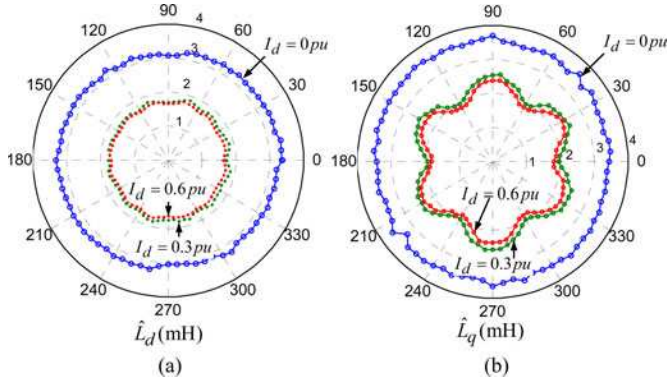

Fig. 17. Estimated $d-q$ axis inductances in an electrical cycle. (a) Estimated d-axis inductance and (b) estimated q-axis inductance.

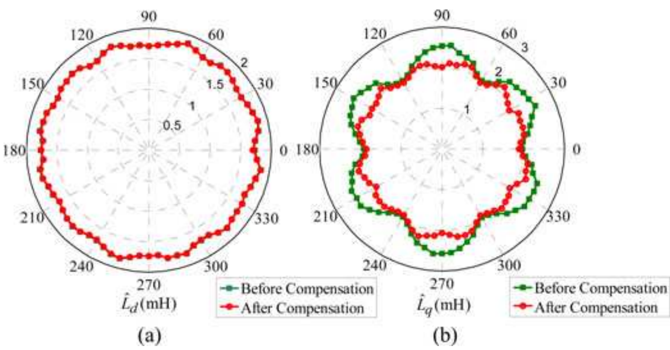

Fig. 18. Estimated $d-q$ axis inductances in an electrical cycle before and after compensation. (a) Estimated d-axis inductance before and after compensation ($I_d = 0.3$ p.u.), (b) estimated q-axis inductance before and after compensation ($I_d = 0.3$ p.u.).

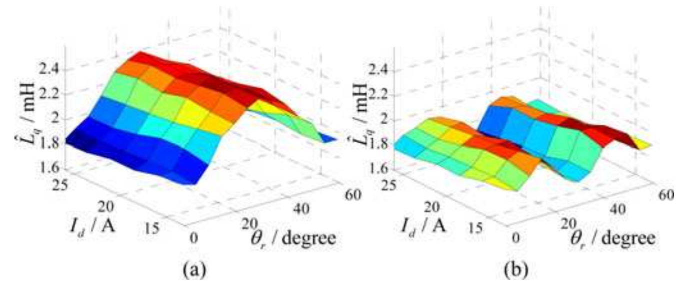

Fig. 19. Experimental results of the influence of cross-coupling effects. (a) Before compensation and (b) after compensation.

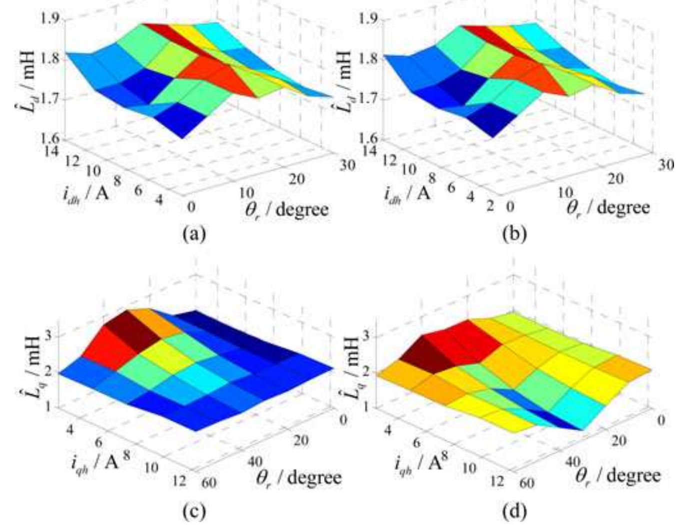

Fig. 20. Experimental results of estimated inductance considering different injected HF currents. (a) Estimated L_d before compensation, (b) estimated L_d after compensation, (c) estimated L_q before compensation, and (d) estimated L_q after compensation.

$\theta_r = k\pi/6, k \in \{0, 1, 2, 3, 4, 5\}$. The experimental results verify the influence of the HF equivalent resistance on the L_d and L_q estimation errors, which is analyzed in Section III.

Fig. 18 shows the estimated $d-q$ axis inductances before and after the model-based compensation. The compensated d-axis inductance is almost the same as the uncompensated value in Fig. 18(a) because the influence of nonlinearities is relatively small. For q-axis inductance identification results, the effect of compensation is distinct. However, there are still small fluctuations in the compensated identification results. But the identification accuracy is improved by the model-based compensation. It should be noted that the parameters of the nonlinearity model need to be accurate. The coefficients used in the compensation model are $I_d = 0.3$ p.u., $k = 0.6$, $\Delta U = 17.2$ V, and $R_s = 0.135\ \Omega$.

The cross-coupling effects between the two axes are analyzed by injecting constant current in one axis and high-frequency signal in the other. Fig. 19 shows the identified q-axis inductance when the fundamental current component in d-axis varies. A constant current injected in d-axis determining its effect on q-axis inductance does not produce torque. However it is not the same for q-axis, when a constant current in q-axis is required to identify cross-saturation effect in d-axis because the machine tends to rotate due to the alignment torque. The experimental results indicate that the cross-coupling effects does not affect the inductance identification obviously at the same rotor position on the tested PMSM since the estimated q-axis inductance almost keeps constant when the injected constant current in d-axis varies. The cross-coupling effects impacting on the identification depend on different electric machine designs.

The experimental results considering different injected HF currents are shown in Fig. 20. It can be seen that the identified inductances, especially for the q-axis inductance, tend to be affected less by the inverter nonlinearities since the increase of signal to noise ratio. But the limit of the injected HF current exists avoid the rotor vibrating when identify the q-axis inductance particularly. The estimated d-axis inductance almost stays the same after the model compensation since the VSI nonlinearity effect imposes on d-axis slightly. If the injected HF current is too large, overcompensation might produce due to the small-signal model cannot be guaranteed under this large HF current injection. The maximum variation percentage of d-axis inductance decreases from 3.08% to 2.90% and the maximum variation percentage of q-axis inductance decreases from 32.31% to 12.77% after compensation.

Fig. 21 shows the measured result of a-phase inductance using the inductance bridge method. The measured phase

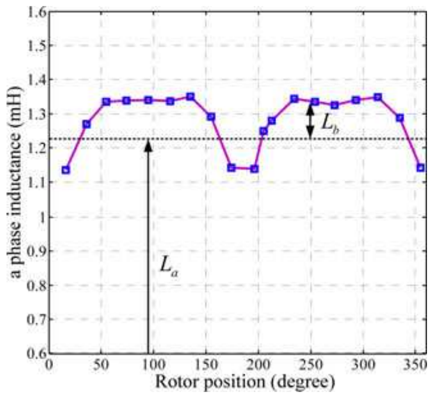

Fig. 21. Measured result of a-phase inductance using the inductance bridge method.

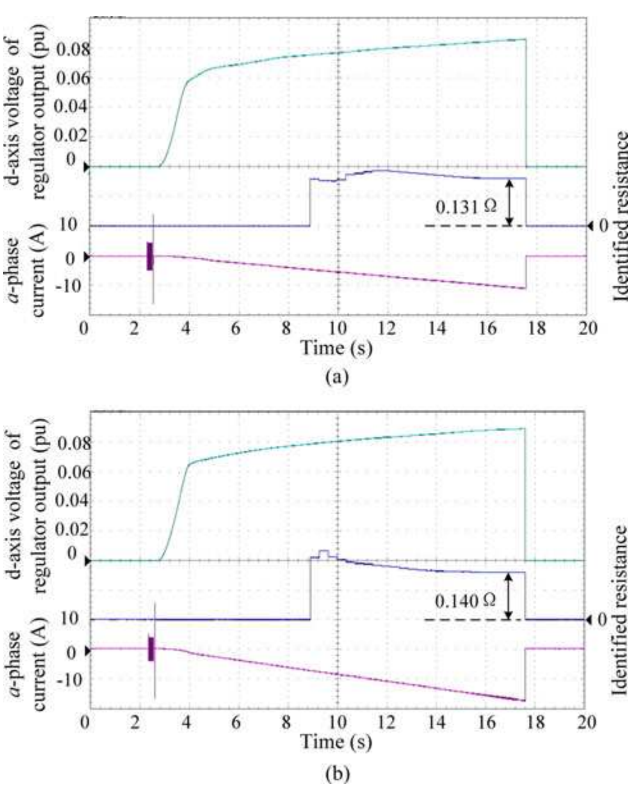

Fig. 22. Experimental waveforms of the stator resistance identification. (a) $\theta_r = 108^\circ$ and (b) $\theta_r = 60^\circ$.

inductance can be converted into d-q axes and the measured $L_d = 1.5(L_a - L_b) = 1.703$ mH and $L_q = 1.5(L_a + L_b) = 2.025$ mH that can be a reference to verify the proposed method.

Fig. 22 shows the experimental waveforms of the stator resistance identification by adopting the proposed linear regression. From top to bottom, the d-axis voltage of the current regulator output, the identified resistance and the a-phase current are given. Fig. 23 shows the identified stator resistance at different initial rotor positions. Fig. 23(a) shows the identified resistance is 0.131 Ω at $\theta_r = 108^\circ$ and Fig. 23(b) shows the identified resistance is 0.140 Ω at $\theta_r = 60^\circ$. The average deviation of the proposed method is 3.35%. The phase voltage error ΔU is 17.2 V in this paper. The voltage drop of the nominal resistance

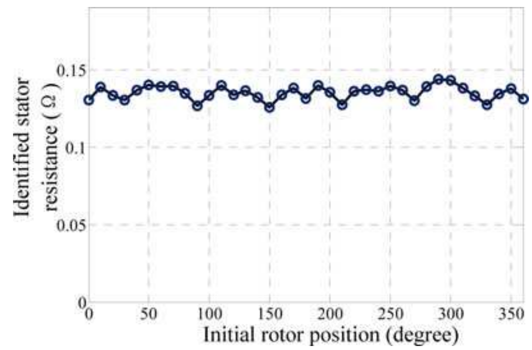

Fig. 23. Identified stator resistance at different rotor positions.

0.135 Ω is 5.022 V at rated current 37.2 A. Although the resistance voltage drop is far smaller than the phase voltage error, the latter can still be eliminated using linear regression no matter how large it is. In practical applications, the saturation value ΔU will vary slightly with the current considering the nonideal properties of the device.

V. Conclusion

A novel self-commissioning methodology for PMSMs at standstill using a VSI fed drive was proposed. The influence of inverter nonlinearities including the parasitic capacitance on the identification at different rotor positions was analyzed. The injected d-axis dc current reduces the influence of inverter nonlinearities effectively during the inductance parameter identification. Furthermore, the nonlinearity model adopted to compensate the identified inductances enhances the estimation accuracy. During the proposed stator resistance identification, the linearly increasing current is injected to utilize the multipoint information. The linear regression method is a promising and robust way to resist the influence of inverter nonlinearities. In practical applications, the time consumed for the self-commissioning can be adjusted by tuning the change rate of the injected signals. The experimental results show that the proposed self-commissioning method is qualified for general-purpose drive applications.

Appendix

The derivations of (11) and (12) are provided in the following. The current response in the $d{-}q$ axes has been given as (10). Transform (10) into the a-b-c stationary reference frame

$$\begin{aligned}\begin{bmatrix} i_a \\ i_b \\ i_c \end{bmatrix} &= \begin{bmatrix} \cos\theta_r & -\sin\theta_r & 1 \\ \cos(\theta_r - 2\pi/3) & -\sin(\theta_r - 2\pi/3) & 1 \\ \cos(\theta_r + 2\pi/3) & -\sin(\theta_r - 2\pi/3) & 1 \end{bmatrix} \cdot \begin{bmatrix} i_d \\ i_q \\ i_0 \end{bmatrix} \\ &= \begin{bmatrix} i_h \cos\theta_r \\ i_h \cos(\theta_r - 2\pi/3) \\ i_h \cos(\theta_r + 2\pi/3) \end{bmatrix} + \begin{bmatrix} I_d \cos\theta_r \\ I_d \cos(\theta_r - 2\pi/3) \\ I_d \cos(\theta_r + 2\pi/3) \end{bmatrix} \\ &= \begin{bmatrix} i_{ah} \\ i_{bh} \\ i_{ch} \end{bmatrix} + \begin{bmatrix} i_{af} \\ i_{bf} \\ i_{cf} \end{bmatrix} \end{aligned} \tag{A1}$$

where the current expression can be divided into a HF term and a fundamental term (dc current component) in arbitrary phase, such as $i_a = i_{ah} + i_{af}$.

The phase voltage error can be expressed as [38]

$$\Delta u_{\text{err}-x} = 2\Delta U \times \left(\frac{1}{1+e^{-ki_f}} - \frac{1}{2}\right) \tag{A2}$$

which is a sigmoid function.

Then, if the HF component is imposed on the fundamental component, the voltage error can be expressed as

$$\Delta u_{\text{err}-x} \approx f(i_{xf}) + f'(i_{xf}) \cdot i_{xh} \approx \text{sign}(i_{xf}) \cdot \Delta U + R_{xh} \cdot i_{xh} \tag{A3}$$

where

$$R_{xh} = f'(i_{xf}) = \frac{2\Delta U \cdot k \cdot e^{-ki_{xf}}}{(1+e^{-ki_{xf}})^2}. \tag{A4}$$

(A4) is the phase HF equivalent resistance. And the HF equivalent resistance in the $d-q$ axes can be deduced in the following. The HF voltage drop in the *a-b-c* axes can be expressed as

$$\begin{bmatrix} \Delta U_{\text{err}-Ah} \\ \Delta U_{\text{err}-Bh} \\ \Delta U_{\text{err}-Ch} \end{bmatrix} = \begin{bmatrix} i_{ah} \\ i_{bh} \\ i_{ch} \end{bmatrix} \cdot [\, R_{ah} \quad R_{bh} \quad R_{ch} \,] = \begin{bmatrix} R_{ah} \cdot i_h \cos\theta_r \\ R_{bh} \cdot i_h \cos\left(\theta_r - \frac{2}{3}\pi\right) \\ R_{ch} \cdot i_h \cos\left(\theta_r + \frac{2}{3}\pi\right) \end{bmatrix}. \tag{A5}$$

Transform (A5) into the $d-q$ rotating frame

$$\begin{bmatrix} \Delta U_{\text{err}-dh} \\ \Delta U_{\text{err}-qh} \\ \Delta U_{\text{err}-0h} \end{bmatrix} = \frac{2}{3} \begin{bmatrix} \cos\theta_r & \cos\left(\theta_r - \frac{2}{3}\pi\right) & \cos^2\left(\theta_r + \frac{2}{3}\pi\right) \\ -\sin\theta_r & -\sin\left(\theta_r - \frac{2}{3}\pi\right) & -\sin\left(\theta_r + \frac{2}{3}\pi\right) \\ \frac{1}{2} & \frac{1}{2} & \frac{1}{2} \end{bmatrix} \cdot \begin{bmatrix} \Delta U_{\text{err}-Ah} \\ \Delta U_{\text{err}-Bh} \\ \Delta U_{\text{err}-Ch} \end{bmatrix} \tag{A6}$$

and the HF voltage error in the $d-q$ axes can be expressed as

$$\begin{cases} \Delta U_{\text{err}-dh} = \frac{2}{3} i_h \left[R_{ah}\cos^2(\theta_r) + R_{bh}\cos^2\left(\theta_r - \frac{2}{3}\pi\right) + R_{ch}\cos^2\left(\theta_r + \frac{2}{3}\pi\right)\right] \\ \Delta U_{\text{err}-qh} = \frac{1}{3} i_h \left[R_{ah}\sin(2\theta_r) + R_{bh}\sin 2\left(\theta_r - \frac{2}{3}\pi\right) + R_{ch}\sin 2\left(\theta_r + \frac{2}{3}\pi\right)\right]. \end{cases} \tag{A7}$$

Rewrite (A7) into (A8)

$$\begin{cases} \Delta U_{\text{err}-dh} = i_h \cdot R_{dh} \\ \Delta U_{\text{err}-qh} = i_h \cdot R_{qh} \end{cases} \tag{A8}$$

where

$$\begin{cases} R_{dh} = \frac{2}{3}\left[R_{ah}\cos^2(\theta_r) + R_{bh}\cos^2\left(\theta_r - \frac{2}{3}\pi\right) + R_{ch}\cos^2\left(\theta_r + \frac{2}{3}\pi\right)\right] \\ R_{qh} = \frac{1}{3}\left[R_{ah}\sin(2\theta_r) + R_{bh}\sin 2\left(\theta_r - \frac{2}{3}\pi\right) + R_{ch}\sin 2\left(\theta_r + \frac{2}{3}\pi\right)\right]. \end{cases} \tag{A9}$$

References

[1] D. Paulus, J. Stumper, and R. Kennel, "Sensorless control of synchronous machines based on direct speed and position estimation in polar stator-current coordinates," *IEEE Trans. Power Electron.*, vol. 28, no. 5, pp. 2503–2513, May 2013.

[2] S. Chaithongsuk, B. Nahid-Mobarakeh, J. P. Caron, N. Takorabet, and F. Meibody-Tabar, "Optimal design of permanent magnet motors to improve field-weakening performances in variable speed drives," *IEEE Trans. Ind. Electron.*, vol. 59, no. 6, pp. 2484–2494, Jun. 2012.

[3] W. Wang, M. Cheng, B. Zhang, Y. Zhu, and S. Ding, "A fault-tolerant permanent-magnet traction module for subway applications," *IEEE Trans. Power Electron.*, vol. 29, no. 4, pp. 1646–1658, Apr. 2014.

[4] P. B. Reddy, A. M. El-Refaie, J. K. Tangudu, and T. M. Jahns, "Comparison of interior and surface PM machines equipped with fractional-slot concentrated windings for hybrid traction applications," *IEEE Trans. Energy Convers.*, vol. 27, no. 3, pp. 593–602, Sep. 2012.

[5] T. Miyajima, H. Fujimoto, and M. Fujitsuna, "A precise model-based design of voltage phase controller for IPMSM," *IEEE Trans. Power Electron.*, vol. 28, no. 12, pp. 5655–5664, Dec. 2013.

[6] S. Kim and J. Seok, "Maximum voltage utilization of IPMSMs using modulating voltage scalability for automotive applications," *IEEE Trans. Power Electron.*, vol. 28, no. 12, pp. 5639–5646, Dec. 2013.

[7] K. Jezernik, J. Korelic, and R. Horvat, "PMSM sliding mode FPGA-based control for torque ripple reduction," *IEEE Trans. Power Electron.*, vol. 28, no. 7, pp. 3549–2013, Jul. 2013.

[8] S. Po-ngam and S. Sangwongwanich, "Stability and dynamic performance improvement of adaptive full-order observers for sensorless PMSM drive," *IEEE Trans. Power Electron.*, vol. 27, no. 2, pp. 588–600, Feb. 2012.

[9] C. Y. Yu, J. Tamura, D. D. Reigosa, and R. D. Lorenz, "Position self-sensing evaluation of a FI-IPMSM based on high-frequency signal injection methods," *IEEE Trans. Ind. Appl.*, vol. 49, no. 2, pp. 880–888, Mar./Apr. 2013.

[10] Z. Wang, K. Lu, and F. Blaabjerg, "A simple startup strategy based on current regulation for back-EMF-based sensorless control of PMSM," *IEEE Trans. Power Electron.*, vol. 27, no. 8, pp. 3817–3825, Aug. 2012.

[11] A. Khlaief, M. Bendjedia, M. Boussak, and M. Gossa, "A nonlinear observer for high-performance sensorless speed control of IPMSM drive," *IEEE Trans. Power Electron.*, vol. 27, no. 6, pp. 290–297, Jun. 2012.

[12] A. Sarikhani and O. A. Mohammed, "Sensorless control of PM synchronous machines by physics-based EMF observer," *IEEE Trans. Energy Convers.*, vol. 27, no. 4, pp. 1009–1017, Dec. 2012.

[13] Y. Zhao, W. Qiao, and L. Wu, "An adaptive quasi-sliding-mode rotor position observer-based sensorless control for interior permanent magnet synchronous machines," *IEEE Trans. Power Electron.*, vol. 28, no. 12, pp. 5618–5629, Dec. 2013.

[14] G. Wang, Z. Li, G. Zhang, Y. Yu, and D. Xu, "Quadrature PLL-based high-order sliding mode observer for IPMSM sensorless control with online MTPA control strategy," *IEEE Trans. Energy Convers.*, vol. 28, no. 1, pp. 214–224, Mar. 2013.

[15] M. Hinkkanen, T. Tuovinen, L. Harnefors, and J. Luomi, "A combined position and stator-resistance observer for salient PMSM drives: design and stability analysis," *IEEE Trans. Power Electron.*, vol. 27, no. 2, pp. 601–609, Feb. 2012.

[16] M. A. G. Moghadam and F. Tahami, “Sensorless control of PMSMs with tolerance for delays and stator resistance uncertainties,” *IEEE Trans. Power Electron.*, vol. 28, no. 3, pp. 1391–1399, Mar. 2013.

[17] A. Bechouche, H. Sediki, D. O. Abdeslam, and S. Haddad, “A novel method for identifying parameters of induction motors at standstill using ADALINE,” *IEEE Trans. Energy Convers.*, vol. 27, no. 1, pp. 105–116, Mar. 2012.

[18] Y. He, Y. Wang, Y. Feng, and Z. Wang, “Parameter identification of an induction machine at standstill using the vector constructing method,” *IEEE Trans. Power Electron.*, vol. 27, no. 2, pp. 905–915, Feb. 2012.

[19] A. Cavagnino, M. Lazzari, F. Profumo, and A. Tenconi, “Axial flux interior PM synchronous motor: parameters identification and steady-state performance measurements,” *IEEE Trans. Ind. Appl.*, vol. 36, no. 6, pp. 1581–1588, Nov./Dec. 2000.

[20] T. L. Vandoorn, F. M. De Belie, T. J. Vyncke, J. A. Melkebeek, and P. Lataire, “Generation of multisinusoidal test signals for the identification of synchronous-machine parameters by using a voltage-source inverter,” *IEEE Trans. Ind. Electron.*, vol. 57, no. 1, pp. 430–439, Jan. 2010.

[21] A. Boglietti, A. Cavagnino, and M. Lazzari, “Experimental high-frequency parameter identification of AC electrical motors,” *IEEE Trans. Ind. Appl.*, vol. 43, no. 1, pp. 23–29, Jan./Feb. 2007.

[22] E. C. Bortoni and J. A. Jardini, “A standstill frequency response method for large salient pole synchronous machines,” *IEEE Trans. Energy Convers.*, vol. 19, no. 4, pp. 687–691, Dec. 2004.

[23] R. Dutta and M. F. Rahman, “A comparative analysis of two test methods of measuring d- and q-axes inductances of interior permanent- magnet machine,” *IEEE Trans. Magn.*, vol. 42, no. 11, pp. 3712–3718, Nov. 2006.

[24] M. A. Arjona, M. Cisneros-González, and C. Hernández, “Parameter estimation of a synchronous generator using a sine cardinal perturbation and mixed stochastic-deterministic algorithms,” *IEEE Trans. Ind. Electron.*, vol. 57, no. 1, pp. 430–439, Jan. 2010.

[25] K. M. Rahman and S. Hiti, “Identification of machine parameters of a synchronous motor,” *IEEE Trans. Ind. Appl.*, vol. 41, no. 2, pp. 557–565, Mar./Apr. 2005.

[26] M. Cisneros-Gonzalez, C. Hernandez, R. Morales-Caporal, E. Bonilla-Huerta, and M. A. Arjona, “Parameter estimation of a synchronous-generator two-axis model based on the standstill chirp test,” *IEEE Trans. Energy Convers.*, vol. 28, no. 1, pp. 44–51, Mar. 2013.

[27] M. A. Herrán, J. R. Fischer, S. A. González, M. G. Judewicz, and D. O. Carrica, “Adaptive dead-time compensation for grid-connected PWM inverters of single-stage PV systems,” *IEEE Trans. Power Electron.*, vol. 28, no. 6, pp. 2816–2825, May 2013.

[28] H. S. Che, E. Levi, M. Jones, W. Hew, and N. A. Rahim, “Current control methods for an asymmetrical six-phase induction motor drive,” *IEEE Trans. Power Electron.*, vol. 29, no. 1, pp. 407–417, Jan. 2014.

[29] K. Liu and Z. Q. Zhu, “Online estimation of the rotor flux linkage and voltage-source inverter nonlinearity in permanent magnet synchronous machine drives,” *IEEE Trans. Power Electron.*, vol. 29, no. 1, pp. 418–427, Jan. 2014.

[30] S. Morimoto, M. Sanada, and Y. Takeda, “Mechanical sensorless drives of IPMSM with online parameter identification,” *IEEE Trans. Ind. Appl.*, vol. 42, no. 5, pp. 1241–1248, Sep./Oct. 2006.

[31] G. Stojcic and T. M. Wolbank, “Detection of defects in stator winding of inverter fed induction machines,” in *Proc. IEEE Int. Elect. Machines Drives Conf. (IEMDC)*, 2013, pp. 111–116.

[32] G. Pellegrino, P. Guglielmi, E. Armando, and R. I. Bojoi, “Self-commissioning algorithm for inverter nonlinearity compensation in sensorless induction motor drives,” *IEEE Trans. Ind. Appl.*, vol. 46, no. 4, pp. 1416–1424, Jul./Aug. 2010.

[33] S. A. Odhano, A. Boglietti, R. Bojoi, and E. Armando, “Unified direct-flux vector control of induction motor self-commissioning drive with analysis of parameter detuning effects,” in *Proc. IEEE Energy Convers. Congr. Expo.*, 2013, pp. 2071–2078.

[34] J. Holtz, “Acquisition of position error and magnet polarity for sensorless control of PM synchronous machines,” *IEEE Trans. Ind. Appl.*, vol. 44, no. 4, pp. 1172–1180, Jul./Aug. 2008.

[35] Y. Park and S. K. Sul, “A novel method utilizing trapezoidal voltage to compensate for inverter nonlinearity,” *IEEE Trans. Power Electron.*, vol. 27, no. 12, pp. 4837–4846, Dec. 2012.

[36] J. M. Guerrero, M. Leetmaa, F. Briz, A. Zamarrón, and R. D. Lorenz, “Inverter nonlinearity effects in high-frequency signal-injection-based sensorless control methods,” *IEEE Trans. Ind. Appl.*, vol. 41, no. 2, pp. 618–626, Mar./Apr. 2005.

[37] L. M. Gong and Z. Q. Zhu, “A novel method for compensating inverter nonlinearity effects in carrier signal injection-based sensorless control from positive-sequence carrier current distortion,” *IEEE Trans. Ind. Appl.*, vol. 47, no. 3, pp. 557–565, May/Jun. 2011.

[38] L. M. Gong and Z. Q. Zhu, “Modeling and compensation of inverter nonlinearity effects in carrier signal injection-based sensorless control methods from positive sequence carrier current distortion,” in *Proc. IEEE Energy Convers. Congr. Expo. (ECCE)*, 2010, pp. 3434–3441.

[39] A. T. D. Almeida, F. J. T. E. Ferreira, and J. A. C. Fong, “Standards for efficiency of electric motors,” *IEEE Ind. Appl. Mag.*, vol. 17, no. 2, pp. 12–19, Nov. 2010.

Gaolin Wang (M’13) received the B.S., M.S., and Ph.D. degrees in electrical engineering from Harbin Institute of Technology (HIT), Harbin, China, in 2002, 2004, and 2008, respectively.

In 2009, he joined the Department of Electrical Engineering, HIT as a Lecturer, where he has been an Associate Professor of electrical engineering since 2012. From 2009 to 2012, he was a Postdoctoral Fellow in Shanghai STEP Electric Corporation. He has authored more than 30 technical papers published in journals and conference proceedings. He is the holder of seven Chinese patents. His current major research interests include permanent magnet synchronous motor drives, high-performance direct-drive for traction system, position sensorless control of ac motors, and efficiency optimization control of Interior PMSM.

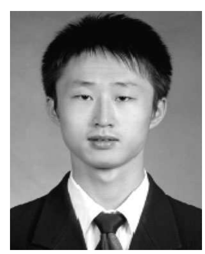

Lizhi Qu received the B.S. degree in electrical engineering from Harbin Institute of Technology (HIT), Harbin, China, in 2013. He is currently working toward the M.S. degree in power electronics and electrical drives in the School of Electrical Engineering and Automation, HIT.

His current research interests include interior permanent magnet synchronous motor drives and efficiency optimization control.

Hanlin Zhan received the B.S. degree in electrical engineering from Harbin Institute of Technology (HIT), Harbin, China, in 2012. He is currently working toward the M.S. degree in power electronics and electrical drives in the School of Electrical Engineering and Automation, HIT.

His current research interests include permanent magnet synchronous motor drives and parameter identification.

Jin Xu received the B.S. degree in electrical engineering from Harbin Institute of Technology, Harbin (HIT), China, in 2013. He is currently working toward the M.S. degree in power electronics and electrical drives in the School of Electrical Engineering and Automation, HIT.

His current research interests include direct-drive permanent magnet synchronous motor control and position sensorless control.

Li Ding received the B.S. degree in electrical engineering from Shanghai University, Shanghai, China, in 2013. He is currently woking toward the M.S. degree in power electronics and electrical drives in the School of Electrical Engineering and Automation, Harbin Institute of Technology.

His current research interests include permanent magnet synchronous motor drives and position sensorless control.

Guoqiang Zhang received the B.S. degree in electrical engineering from Harbin Engineering University, Harbin, China, in 2011, and the M.S. degree in electrical engineering from Harbin Institute of Technology (HIT), Harbin, in 2013. He is currently working toward the Ph.D. degree in power electronics and electrical drives in the School of Electrical Engineering and Automation, HIT.

His current research interests include permanent magnet synchronous motor drives and position sensorless control.

Dianguo Xu (M'97–SM'12) received the B.S. degree in control engineering from Harbin Engineering University, Harbin, China, in 1982, and the M.S. and Ph.D. degrees in electrical engineering from Harbin Institute of Technology (HIT), in 1984 and 1989, respectively.

In 1984, he joined the Department of Electrical Engineering, HIT as an Assistant Professor. Since 1994, he has been a Professor in the Department of Electrical Engineering, HIT. He was the Dean of School of Electrical Engineering and Automation, HIT from 2000 to 2010. He is currently the Assistant President of HIT. His research interests include renewable energy generation technology, power quality mitigation, sensorless vector controlled motor drives, and high-performance PMSM servo system. He published more than 600 technical papers.

Dr. Xu is an Associate Editor for the IEEE TRANSACTIONS ON INDUSTRIAL ELECTRONICS. He serves as the Chairman of IEEE Harbin Section.